# Ferromagnetic composite with stress-insensitive magnetic permeability: Compensation of stress-induced anisotropies

Junming Gou,[1,2] Xiaolian Liu,[1,3] Changsheng Zhang,[4] Guangai Sun,[4] Yinuo Shi,[5] Jie Wang,[5] Huaxiong Chen,[6] Tianyu Ma,[1,*] and Xiaobing Ren[1]

[1]*Frontier Institute of Science and Technology and State Key Laboratory for Mechanical Behavior of Materials, Xi'an Jiaotong University, Xi'an 710049, China*

[2]*School of Materials Science and Engineering, Zhejiang University, Hangzhou 310027, China*

[3]*Innovation Center for Advanced Materials, Hangzhou Dianzi University, Hangzhou 310012, China*

[4]*Key Laboratory for Neutron Physics of Chinese Academy of Engineering Physics, Institute of Nuclear Physics and Chemistry, Mianyang 621999, China*

[5]*Department of Engineering Mechanics, School of Aeronautics and Astronautics, Zhejiang University, Hangzhou 310027, China*

[6]*National Center for Science and Technology Evaluation, Beijing 100081, China*

(Received 18 July 2018; revised manuscript received 29 September 2018; published 19 November 2018)

Single-phase ferromagnets show deterioration of magnetic permeability when operating under a prestress due to the stress-induced anisotropy, which is a serious restriction for soft magnets. However, technologically, it is highly desired that soft magnets can maintain stable permeability under high stress. Here we report that a ferromagnetic Fe-Ga composite exhibits nearly unchanged magnetic permeability and coercivity even when subjected to compressive prestress as high as 200 MPa. Such stress-insensitive magnetic properties stem from the compensation of stress-induced anisotropies between the two ferromagnetic components with opposite magnetostriction signs ($\lambda > 0$ for the bcc phase and $\lambda < 0$ for the fcc phase). The magnetomechanical measurements and phase field simulations revealed that the stress-induced domain switching pathways are competitive between the bcc and the fcc phases, ruling out the prestress influence on magnetization. The present finding may provide a general recipe for designing soft magnets with stable magnetic properties under high stress.

DOI: 10.1103/PhysRevMaterials.2.114406

## I. INTRODUCTION

Soft magnets are magnetic materials with high permeability, low coercivity, and low hysteresis loss [1,2], which can be used to amplify the flux density generated by a magnetic field. They play vital roles in both power generation and conversion for electrical and electronic equipment [3–5]. In most applications, soft magnets are fixed to the devices or surrounded by windings, hence extra stress is induced. The extra prestress leads to a common restriction for soft magnets that the working permeability (the ratio of magnetic induction to the applied field) is much lower than that of the stress-free conditions. For instance, when fixed to the devices, the Mn-Zn soft ferrite can suffer 60% permeability loss in comparison with the fresh material [6]. Consequently, soft magnets with stress-insensitive permeability are highly desired for practical applications.

The permeability loss under stress originates from the stress-induced extra anisotropy (the magnetoelastic anisotropy $K_\sigma$ that has the following relation to the saturation magnetostriction constant $\lambda_s$ and stress $\sigma$ : $K_\sigma = -3/2\lambda_s\sigma$) due to the magnetoelastic coupling [1,2]. The stress-driven motion of non-180° magnetic domain walls (DWs) changes the initial magnetic state as well as the subsequent magnetization process under external magnetic fields. When applying a uniaxial compressive stress on a cylinder rod with positive $\lambda_s$ (for example, Fe or Tb-Dy-Fe alloys [7–9]) or applying a uniaxial tensile stress on a cylinder rod with negative $\lambda_s$ (for example, Ni [10]), the flux density within a pick-up coil circulating the rod reduces because the magnetic domains tend to reorient perpendicularly to the rod axis. The obtained permeability during the subsequent magnetization process becomes smaller than that of the stress-free conditions, as the uniaxial magnetic field tends to switch the magnetic domains to be parallel to the rod axis [11]. That is why the ferromagnets with positive magnetostriction suffer permeability loss under high compressive stress and the ones with negative magnetostriction suffer permeability loss under high tensile stress. Therefore, to avoid stress-induced permeability loss, it is usual to reduce the magnetostriction and the associated stress-induced anisotropy (SIA) to zero. Successful examples include Fe-Ni and Fe-Si-Al alloys [12–15], for which the $\lambda_s$ can be reduced to zero through strictly placing them at specific compositions.

If a ferromagnetic composite contains two components with opposite magnetostriction signs and proper volume fractions, the SIAs of the individual component could be compensated, and the prestress-induced permeability loss can then be avoided. Here we report that a proof-of-principle reference, a Fe-Ga composite containing both negative and positive magnetostriction components, indeed exhibits such

*matianyu@xjtu.edu.cn

 

appealing behaviors, and its permeability and coercivity keep nearly unchanged under compressive prestresses. Fe-Ga alloy, known for its large magnetostriction at low external field, has a diversity of structures with different intrinsic magnetic and magnetostrictive properties and has been the subject of intensive studies [16–30]. When Ga content is within the range from 26 to 28.9 at. %, $Fe_{100-x}Ga_x$ alloys can exhibit disordered bcc A2, ordered bcc B2 and $D0_3$, ordered fcc $L1_2$, and hcp $D0_{19}$ structures [17–21]. Among them, the bcc phases possess positive magnetostriction, and the fcc phase possesses negative magnetostriction. Consequently, it offers an opportunity to fabricate ferromagnetic composites containing both negative and positive magnetostriction phases, which could result in compensation of SIAs. Taking advantage of $D0_3 \rightarrow L1_2$ transformation with slow kinetics [18–21,27–30], it is easy to prepare Fe-Ga composites containing both bcc and fcc phases and to tune the phase fractions through controlling the aging time and temperature. In the following, we shall show that a $Fe_{73}Ga_{27}$ composite prepared by aging the bcc precursor for 3 d at 530 °C indeed exhibits stable permeability even when subjected to a compressive prestress as high as 200 MPa. Based on the magnetomechanical measurements and phase field simulations, the underlying switching pathways of magnetic domains under compressive prestress and magnetic field are revealed, which gives rise to a general recipe to develop soft magnets with stress-insensitive permeability.

## II. EXPERIMENTAL METHODS

$Fe_{73}Ga_{27}$ samples were prepared by arc melting and subsequent copper-mold casting into cylindered rods. Details can be found in our previous work [28]. To remove pores inside, the master rods with diameters of 7 mm were subjected to further solidification on a Bridgman furnace with a pulling rate of ∼10 $\mu$m/s. Three sections with length over 40 mm were cut from the long rod and sealed in quartz tubes for heat treating. One is solution treated for 3 h at 1100 °C, followed by quenching into ice water. Another two solution-treated precursors were subjected to further aging for 3 and 30 d at 530 °C, respectively. After aging, both specimens were finally quenched into oil.

Quasistatic measurements were carried out using the apparatus described in detail previously [31]. Both bias magnetic field and compressive prestress were applied along the rod axis (shown in the inset of Fig. 1). Under different compressive prestresses, the axial magnetic induction was measured as a function of external magnetic field using an integrating device with a pick-up coil. Simultaneously, the axial magnetostriction under different compressive prestresses was measured by the output of a 1-mm-long by 1 mm-wide electrical resistance strain gauge attached to the specimen surface. The piezomagnetic response was detected using the same pick-up coil at different bias magnetic fields. To establish the same initial condition for each measurement, the sample was magnetized up to 0.5 T and demagnetized slowly to the designed bias field. The tests were performed at a low loading rate. The mechanical force is applied through the motion of an upper loading beam driven by the hydraulic pressure, which is under the control of a hydraulic servo-motor system. During loading, speed of the servo motor was fixed. The average structure was characterized by x-ray diffraction (XRD) using a Rigaku diffractometer with Cu $K\alpha$ radiation. To verify the structure stability under high prestress, *in situ* neutron-diffraction technique was used. The neutron-diffraction experiments were carried out on a residual stress neutron diffractometer at China Mianyang Research Reactor with a wavelength of 1.587 Å. A foil sample for transmission electron microscopy (TEM) characterization was prepared by twin-jet electropolishing at temperatures below −30 °C, followed by ion milling for 15 min (beam glancing angle = 6°, beam voltage = 2 kV, and beam current = 5 mA) to remove surface contaminations. TEM characterization was performed using a JEOL JEM-2100F microscope. Magnetic domain structures and electron holography were conducted using the microscope equipped with an electron biprism.

## III. RESULTS AND DISCUSSION

### A. Magnetic properties under different compressive prestresses

Figure 1 shows the magnetic induction and the magnetic permeability ($B/\mu_0 H$) as a function of magnetic field for the as-solution-treated sample and the one aged for 3 d, respectively. These two samples exhibit distinctly different magnetization behaviors when the compressive prestress is applied. The prestress seems to have no influence on the aged sample when compared to the as-solution-treated one. It is clear that the magnetic induction (especially at the low magnetic fields) reduces obviously when applying a uniaxial compressive prestress to the as-solution-treated sample [Fig. 1(a)]. But this phenomenon is not observed for the one aged for 3 d even when a compressive prestress as high as 200 MPa is applied [Fig. 1(d)]. Figures 1(b) and 1(e) reveal the different prestress influences on magnetic permeability ($B/\mu_0 H$) in low magnetic fields between these two samples. With the increase of compressive prestress magnitude, the permeability decreases drastically for the as-solution-treated sample [Fig. 1(b)], but keeps nearly unchanged for the aged sample [Fig. 1(e)]. The stress dependences of coercivity for these two samples [Figs. 1(c) and 1(f)] also showed that the aged sample exhibits much weaker stress-dependent coercivity than that of the as-solution-treated sample. The normalized coercivity reveals this difference more clearly. For the as-solution-treated sample, the coercivity under 200 MPa becomes 4.30 times that under 0 MPa. However, for the aged sample, the coercivity incremental ratio is only 7.7% when 200-MPa prestress is applied. The absolute coercivity for the aged sample under 200 MPa is just 1.25 mT, being comparable to some Co-based soft magnets [5]. In addition, the saturation magnetic induction $B_s$ of the aged sample reaches ∼1.95 T (at 0 MPa), much larger than ∼1.66 T (at 0 MPa) for the as-solution-treated sample. Such stable magnetic permeability and coercivity as well as the large $B_s$ obtained in the aged $Fe_{73}Ga_{27}$ alloy allow potential applications under high prestress conditions.

These results clearly revealed that stress-insensitive magnetic permeability can be obtained in the aged Fe-Ga alloy. In the following, we shall present the microstructure characterizations and magnetomechanical measurements to understand

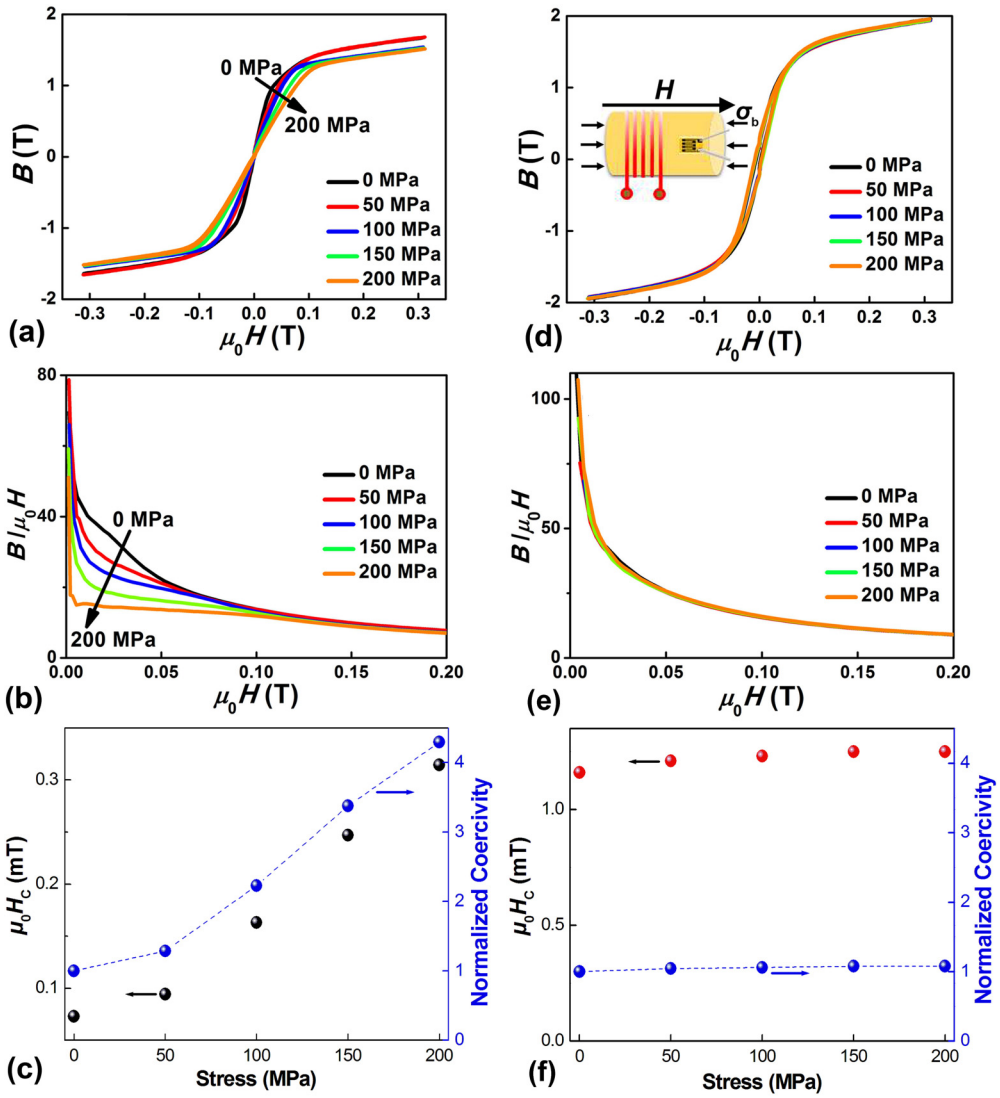


FIG. 1. Magnetization hysteresis loops, the derived magnetic permeability ($B/\mu_0 H$) vs magnetic field, and the stress dependence of coercivity for the as-solution-treated $Fe_{73}Ga_{27}$ sample (a–c) and the one further aged for 3 d at 530 °C (d–f), respectively. For comparison, the coercivity under zero stress conditions is normalized to 1.

why aging the $Fe_{73}Ga_{27}$ alloy can result in such stable magnetic properties under high compressive prestresses.

### B. Microstructure characterizations

The aging treatment changed the microstructure from "bcc averaged" for the as-solution-treated $Fe_{73}Ga_{27}$ into the "bcc + fcc composite" for the 3-d-aged state and into the "main fcc phase" for the 30-d-aged state, as shown in Fig. 2. The XRD patterns were measured on the cross-sectional plane of the rod samples. The as-solution-treated sample exhibits a bcc-averaged structure, which can be determined by the typical {110}, {200}, and {211} reflections for A2 at Bragg angles $2\theta$ of 43.72°, 63.24°, and 80.44° [Fig. 2(a)]. Note that these peaks can also be indexed as the {220}, {400}, and {422} fundamental reflections for the ordered $D0_3$ phase because the as-solution-treated $Fe_{73}Ga_{27}$ has been deemed a phase mixture of A2 + B2 + $D0_3$ [23,29]. Our previous work [29] shows that as-solution-treated $Fe_{73}Ga_{27}$ consists of the nanosized $D0_3$ as the majority. Due to the same magnetostriction sign ($\lambda_s$) for A2, B2, and $D0_3$ phases [18], for easy understanding, it is named as "bcc averaged" hereafter. Meanwhile, after further aging for 3 d at 530 °C, additional reflections {111}, {200}, {220}, and {311} for the $L1_2$ structure appear [Fig. 2(b)]. Our former step-scanned XRD profiles reveal that the volume fraction is ~35% for the $L1_2$ phase and ~65% for the bcc phase [28]. For easy understanding, this sample is named as "bcc + fcc composite" hereafter. Figure 3(a) illustrates the typical bright field image of the sample aged for 3 d. This image was taken by tilting the bcc phase with the [001] zone axis, which exhibits as dark contrast. Along this zone axis, micron-sized fcc grains with bright contrast are revealed, the width is about 0.5 $\mu$m, and the length is about 2 $\mu$m. The fcc grains are clearly segregated and distributed randomly within the bcc matrix. According to the Bain relationship between bcc and fcc phases, multiple fcc variants coexist; i.e., $[001]_{fcc}$, $[1\bar{1}0]_{fcc}$, and $[\bar{1}10]_{fcc}$ will be parallel to the beam if the bcc phase has one of the ⟨100⟩ incidences. It should be addressed

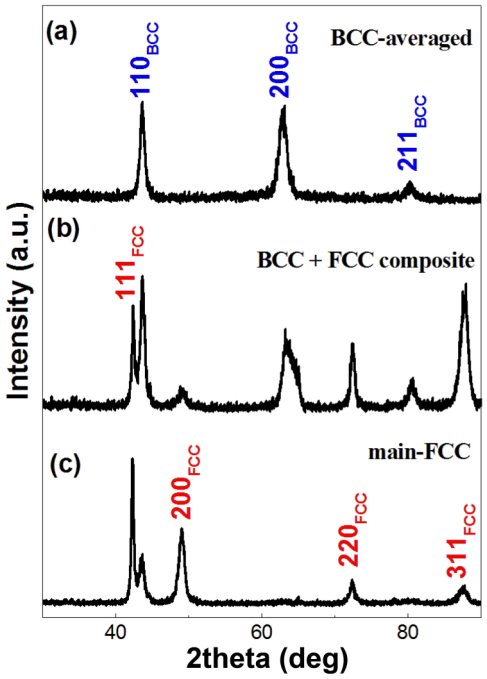


FIG. 2. XRD patterns for the as-solution-treated $Fe_{73}Ga_{27}$ sample (a), the one further aged for 3 d at 530 °C (b), and the one aged for 30 d at 530 °C (c).

that some fcc grains may contain variant pairs due to the shear transformation feature [22]. The crystal structures of different contrasts were verified by the selected area electron diffraction (SAED) patterns in Figs. 3(b) and 3(c), respectively. The ordered $L1_2$ structure is verified by the superlattice reflections at $\{001\}_{fcc}{}^*$ and $\{110\}_{fcc}{}^*$ positions.

Because the $L1_2$ phase has opposite magnetostriction sign to the A2, B2, and $D0_3$ phases (the former has negative magnetostriction and the latter ones have positive magnetostriction) [19–21,27–30], such a composite is what we expected to have stable magnetic permeability under prestress conditions. In addition, it is not surprising that the 3-d-aged sample with bcc + fcc composite structure has larger magnetic induction than the as-quenched one with bcc-averaged structure since the $L1_2$ phase has larger magnetization than A2, B2, and $D0_3$ phases [19–21,27–30]. Ideally, we should distinguish the stress influences on the magnetization process for the single $D0_3$ phase and for the single $L1_2$ phase to understand the above-mentioned stress-insensitive permeability in the Fe-Ga composite. However, it is difficult to evaluate the single phase behaviors due to the facts that (i) A2 and B2 phases always coexist with the $D0_3$ phase even at the solution-treated state for the $Fe_{73}Ga_{27}$ alloy and (ii) although the $L1_2$ phase becomes the majority [the XRD pattern is shown in Fig. 2(c); the intensity of the $\{111\}_{fcc}$ reflection becomes much stronger than that of the $\{110\}_{bcc}$ reflection) the remanent bcc phase still exists even after aging for 30 d at 530 °C because the $D0_3 \rightarrow L1_2$ transformation has very slow kinetics. The complete $D0_3 \rightarrow L1_2$ transformation requires (i) large lattice strain ($\varepsilon_{[001]D03} \sim 0.260$, $\varepsilon_{[010]D03} \sim -0.109$) and (ii) atomic position exchanges [Fe or Ga change sites, for instance, in the $(001)_{D03}$ plane] [22,29]. In general, the shear feature during phase transformation will result in multilayer substructure. Indeed, such substructure is observed in our Fe-Ga composite [Fig. 3(a)]. In fact, the sample aged for 3 d at 530 °C does not reach the equilibrium state. The incomplete $D0_3 \rightarrow L1_2$ transformation may result in intermediate phases, the structure and magnetostrictive properties of which depend on the preparation conditions [22,32,33]. For instance, bcc-like $L6_0$ (modified-$D0_3$) or face-centered-tetragonal (FCT) $D0_{22}$ intermediate phases have been reported [22,32]. Strictly speaking, the aged $Fe_{73}Ga_{27}$ composite may contain multiphases besides $D0_3$ and $L1_2$. For easy understanding, the phases that elongate under the magnetic field are deemed positive magnetostriction components (bcc, and the ones that contract under the magnetic field are deemed negative magnetostriction components (fcc).

Due to the shear feature of the formation of the $L1_2$ phase (as verified in Fig. 3), the compressive stress may damage the structure, i.e., the stability of the composite under high stress is also a concern for practical applications. To check whether the present Fe-Ga composite can tolerate 200-MPa compressive stress or not, we carried out *in situ* neutron-diffraction measurements under a series of compressive prestresses as the neutron diffraction is a powerful technique to detect the structure of the bulk materials. Shown in Fig. 4 are the neutron-diffraction patterns for the bcc + fcc composite sample measured under 0-, 50-, 100-, 150-, and 200-MPa compressive prestresses. Neither the Bragg angle nor the intensity for the $\{111\}_{fcc}/\{220\}_{bcc}$ reflections changes even when subjected to 200 MPa. This demonstrates that the present 3-d-aged Fe-Ga composite has very good structural

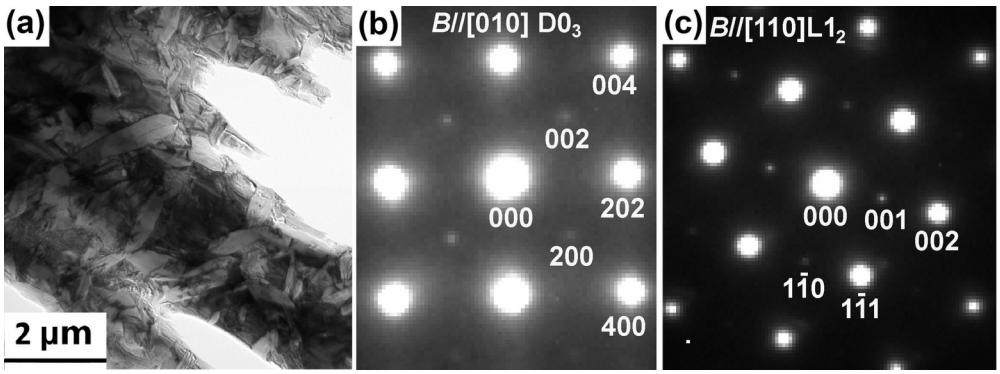


FIG. 3. Bright field image (a) and SAED patterns (b, c) of the $Fe_{73}Ga_{27}$ composite aged for 3 d at 530 °C.

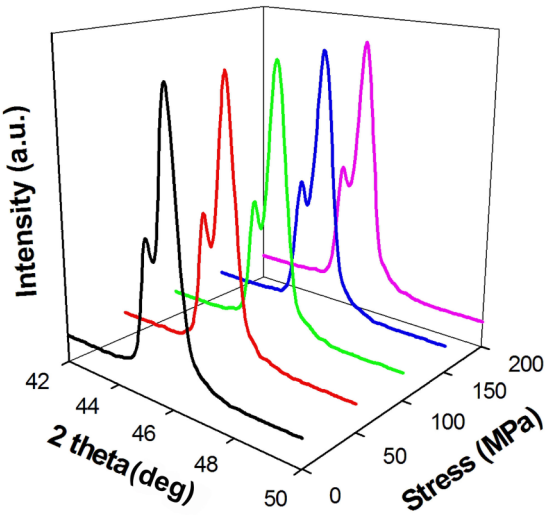


FIG. 4. *In situ* neutron-diffraction patterns of the $Fe_{73}Ga_{27}$ composite measured under different compressive prestresses.

stability under compressive stress despite the fact that it does not reach the equilibrium state thermodynamically. This is due to the fact that the applied stress cannot promote the atomic diffusion process of the $D0_3$ phase at room temperature, which is another requirement of the $D0_3 \rightarrow L1_2$ transformation.

### C. Magnetic domain evolutions

The macroscopic magnetization process under coupled magnetomechanical space originates from the underlying magnetic domain switching pathways (including domain-wall motions and domain rotations). To understand the underlying physical mechanism of the stress-insensitive magnetic permeability in the Fe-Ga composite, we performed further magnetomechanical measurements and phase field simulations to reveal the domain switching pathways, as follows. Because of the difficulties to obtain the single $D0_3$ phase and single $L1_2$ phase in $Fe_{73}Ga_{27}$ alloy, here we use the as-solution-treated specimen to evaluate the domain switching pathways for the bcc phase and use the 30-d-aged specimen (for easy understanding, this sample is named as the "main fcc" hereafter) to evaluate the domain switching pathways for the $L1_2$ phase.

First, the magnetostrictions with different compressive prestresses have been measured for the bcc-averaged, the main fcc, and the bcc + fcc composite samples, as shown in Fig. 5. This measurement helps us to understand the compressive prestress-induced changes in the initial magnetic state and the subsequent magnetization process for the components with positive or negative magnetostrictions. Under stress-free conditions, the parallel magnetostriction due to the motion of non-180° DWs and the rotation of domains towards the field direction is positive for the bcc-averaged sample, is negative for the main-fcc sample, and changes its sign for the bcc + fcc composite sample, respectively. As discussed previously [28], the sign-changed magnetostriction is a net result, i.e., the offset effect between the bcc phase with weaker magnetocrystalline anisotropy and the fcc phase with stronger magnetocrystalline anisotropy. When applying a compressive

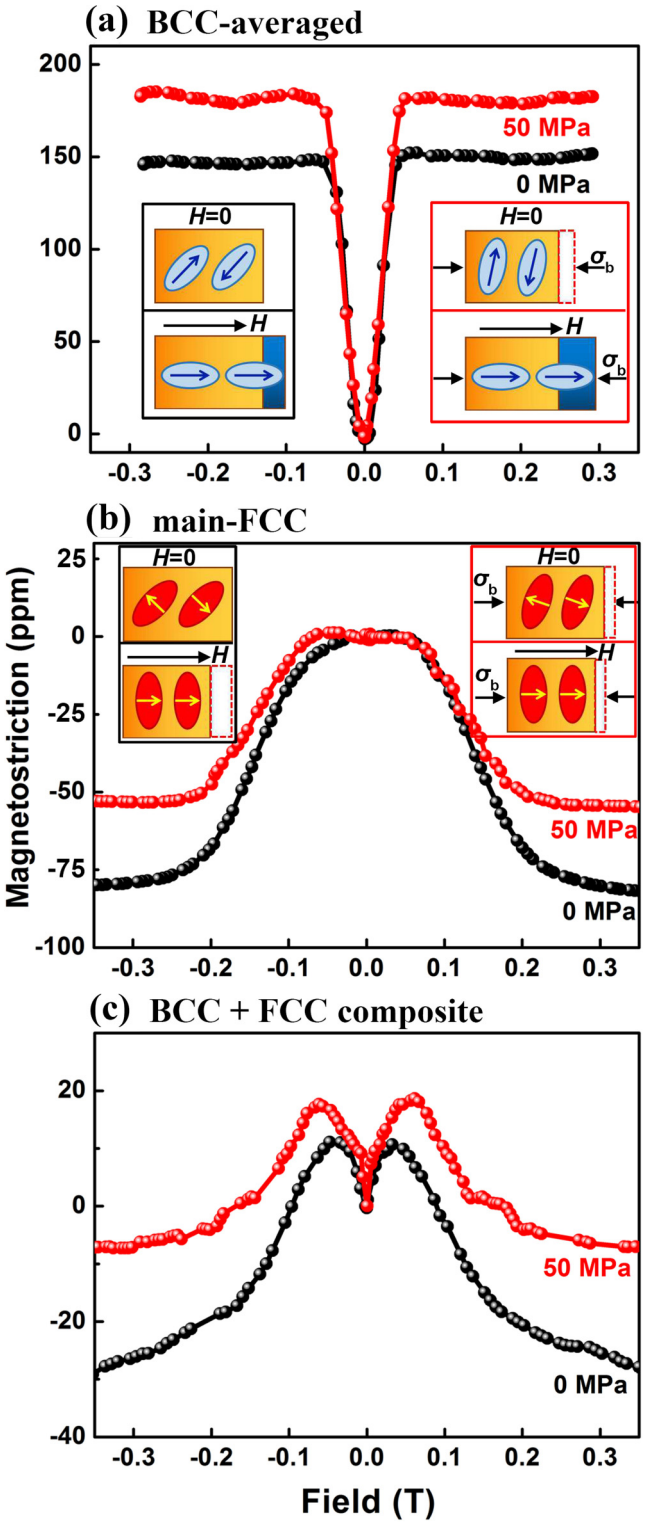


FIG. 5. Magnetostrictions measured under different compressive prestresses for the $Fe_{73}Ga_{27}$ samples. (a) As-solution-treated (bcc-averaged structure), (b) aged for 30 d (main fcc phase), and (c) aged for 3 d (bcc + fcc composite).

prestress of 50 MPa, magnetostriction is enhanced for the bcc-averaged sample ($\lambda_s$ increases from 152 to 182 ppm), but is reduced for the main-fcc sample ($|\lambda_s|$ decreases from 82 to 53 ppm) due to the change of initial magnetic states.

As schematically shown in Fig. 5(a), the compressive prestress drives the magnetic domains of the bcc phase towards the perpendicular direction (via non-180° DW motions), promoting the non-180° domain switching during the subsequent magnetization process as well as the magnetostriction. In contrast, as schematically shown in Fig. 5(b), the compressive prestress drives the magnetic domains of the fcc phase towards the parallel direction (via non-180° DW motions), reducing the non-180° domain switching during the subsequent magnetization process as well as the magnetostriction. These two distinctly different domain switching pathways can also be reflected by Fig. 5(c), where the positive magnetostriction is enhanced and the negative magnetostriction is reduced in comparison with the stress-free condition.

Second, the piezomagnetic responses with different bias magnetic fields have also been measured for the bcc-averaged, the main-fcc, and the bcc + fcc composite samples, as shown in Fig. 6. This measurement helps us to understand the compressive stress-induced magnetic state changes, especially the motions of non-180° DWs. It should be addressed that the motions of magnetic DWs are different for applying a magnetic field or applying a stress: the former can drive the motions of both 180° and non-180° DWs, but the latter can drive the motions of non-180° DWs only [1,2]. In addition, the motion of 180° DWs is prior to that of the non-180° DWs. This is why the piezomagnetic response is stronger at a certain bias magnetic field, at which the motion of 180° DWs has been finished, than that at zero-bias field or saturation-bias field (at which the magnetization cannot be changed by a small stress [11]). For instance, the largest magnetic induction change $\Delta B$ is obtained at a bias field of 0.066 T, much larger than the case for zero field or for 0.3 T, as illustrated in Fig. 6(a). An apparent difference between the bcc-averaged sample and the main-fcc sample is that $\Delta B$ is negative for the former, which means compressive stress reduces the flux density passing through the pick-up coil [Fig. 6(a)]; meanwhile $\Delta B$ is positive for the latter, which means compressive stress enlarges the flux density passing through the pick-up coil [Fig. 6(b)]. These facts, again, indicate that compressive stress acts to offset the parallel magnetic field on the positive magnetostriction phase but acts to assist the parallel magnetic field on the negative magnetostriction phase. For the bcc + fcc composite sample, as illustrated in Fig. 6(c), it is not strange that the piezomagnetic response is pretty weak due to the compensation between the bcc and the fcc components.

Third, a real-space phase field model of ferromagnetic materials based on the Ginzburg-Landau theory is also employed to predict the domain switching under a magnetic field and/or a stress. The simulated microstructure and the magnetic domain structure were derived from the TEM and Lorentz-TEM (L-TEM) characterizations illustrated in Figs. 3 and 7, respectively. Figures 7(a) and 7(b) show in-focus and under-focus L-TEM Fresnel images for the bcc + fcc composite sample, respectively. The under-focus image displays the bright lines of magnetic DWs at different regions, which carve up magnetic domains with various vectors due to spontaneous magnetization. Some DWs are observed at the interface between bcc and fcc phases. To further investigate the difference of magnetic domains between bcc and fcc phases, an electron holography reconstructed phase image obtained from a typical region containing both bcc and fcc phases [Fig. 7(c)] is shown in Fig. 7(d). The density of the contour lines with black-white alternating contrast presents the density of magnetic flux, which is clearly higher in the fcc phase than that in the bcc

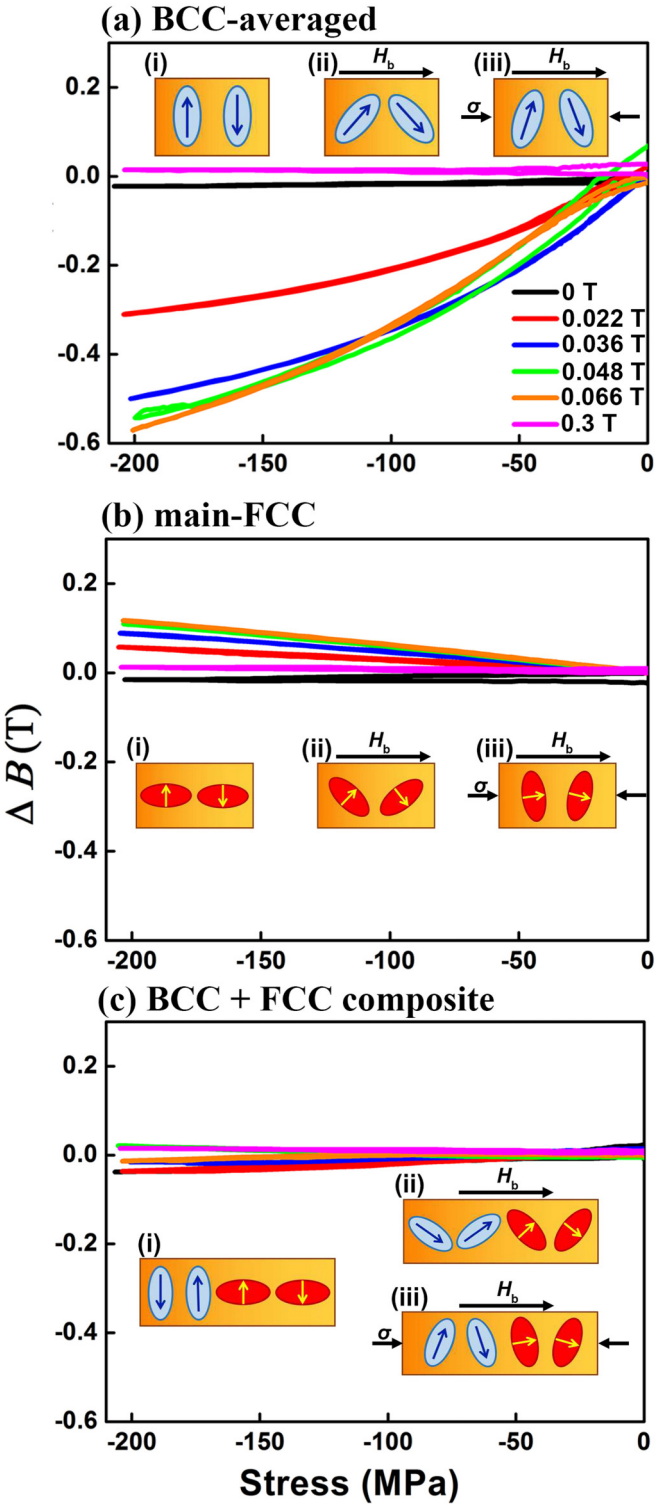


FIG. 6. Piezomagnetic responses ($\Delta B$-$\sigma$ plots) measured under different bias magnetic fields for the $Fe_{73}Ga_{27}$ samples. (a) As-solution-treated (bcc-averaged structure), (b) aged for 30 d (main fcc phase), and (c) aged for 3 d (bcc + fcc composite).

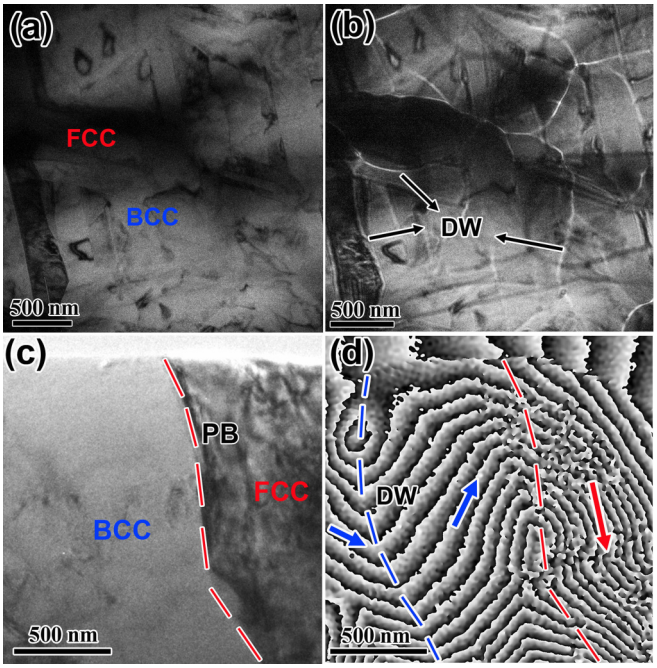


FIG. 7. L-TEM characterizations for the $Fe_{73}Ga_{27}$ composite aged for 3 d at 530 °C. (a, b) In-focus (a) and under-focus (b) Fresnel images. (c, d) In-focus Fresnel image (c) and electron holography reconstructed image (d) for an enlarged region containing both bcc and fcc phases. The contour lines indicate the magnetization distributions and the spacing of the lines provides information regarding the in-plane magnetic flux density. The blue dashed line indicates the domain walls and the red dashed line indicates the phase interfaces. Blue and red arrows indicate the magnetization vectors of bcc and fcc phases, respectively.

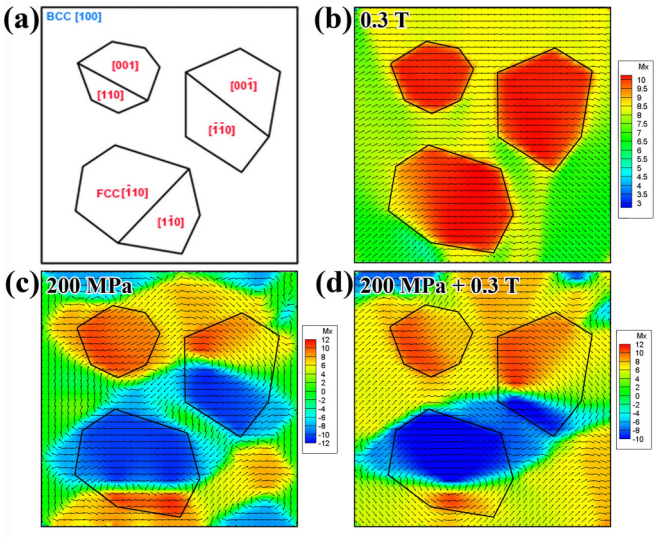


FIG. 8. Magnetic domain evolutions of the $Fe_{73}Ga_{27}$ composite by phase field simulation. (a) Schematic morphology showing the directions of bcc and fcc phases parallel to the eye. (b) Magnetic domain configuration at a horizontal magnetic field of 0.3 T. (c) Magnetic domain configuration by applying 200-MPa compressive stress along the horizontal direction. (d) Magnetic domain configuration at a horizontal magnetic field of 0.3 T with 200-MPa compressive prestress (horizontal).

phase. It is consistent with the fact that the fcc phase has larger magnetization than the bcc phase. A typical 90° DW [as indicated by the dashed blue line in Fig. 7(d)] is observed to separate two adjacent magnetic domains of the bcc phase. The observed fcc region contains magnetic domains with different vectors, referring to the in-plane or out-of-plane magnetizations. The magnetization of one fcc domain is ~45° with respect to the adjacent bcc domain. According to the Bain relationship between bcc and fcc phases, fcc variants with $\langle 110\rangle_{fcc}$ will be formed in the bcc matrix with $\langle 100\rangle_{bcc}$. Thus, the 45° angle between magnetizations of adjacent bcc and fcc domains actually reveals the crystal orientation relationship between them as both of them has the ⟨001⟩ easy axis [34]. Consequently, our phase field simulation was conducted by considering the derived microstructure from these characterizations, where six fcc variants with different crystal axes and magnetization vectors are embedded within the bcc phase, as schematically illustrated in Fig. 8(a). Here, the [100] axis of the bcc phase is perpendicular to the observation plane. Details of the phase field simulation are described in the Appendix. The simulation results directly display the switching pathways of magnetization vectors within the bcc and the fcc phases. Here the modeled microstructure [Fig. 8(a)] is derived from the TEM bright field image, where two $L1_2$ variants are embedded within the matrix bcc phase. Figure 8(b) displays the magnetization vectors at a horizontal magnetic field of 0.3 T without applying prestress. It is clear that most magnetization vectors align along the field direction (from left to right) despite the fact that some of them deviate slightly away from the horizontal direction due to the large stray fields at the sharp phase boundaries. This reflects the rotation of magnetic domains towards the field direction when applying magnetic field only. Figure 8(c) displays the magnetic configurations after applying a compressive prestress of 200 MPa along the horizontal direction. Unlike the fcc phase where most magnetizations align along the horizontal direction, most magnetizations of the bcc phase tend to align along the vertical direction, originating from their different intrinsic magnetostriction features. Figure 8(d) displays the magnetic configurations after applying a 0.3-T horizontal magnetic field with the 200-MPa compressive prestress. Most magnetizations of the bcc phase align along the horizontal direction, the magnetizations within the $L1_2$ variants also tend to align along the horizontal direction.

The above results reveal that the domain switching pathways between the fcc and the bcc phases under compressive prestress are competitive, which is responsible for the stable magnetic permeability under high stress.

### D. Discussion

The above results reveal that the stress-insensitive permeability can be achieved in ferromagnetic composites due to a net result of the stress-induced magnetic state changes for two components with opposite magnetostriction signs. The rule of mixture is schematically summarized in Fig. 9. At the thermal-demagnetized state, all the magnetic domains align along their easy axes. The magnetization increases

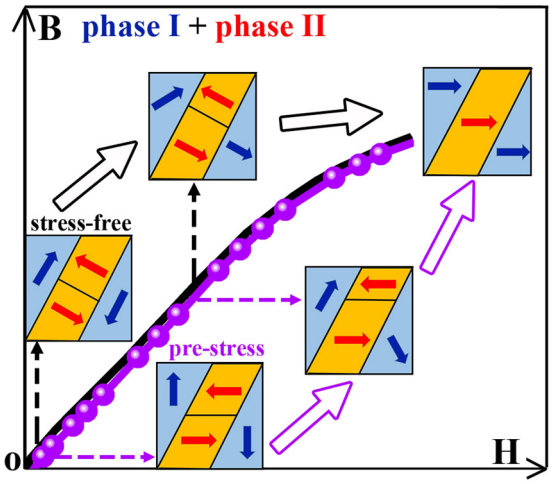


FIG. 9. Schematic figure of obtaining stress-insensitive permeability in a ferromagnetic composite.

when applying external field through the domain switches and reaches saturation with their moments aligning along the field direction (the domain switching pathways are linked by the black arrows). When applying a compressive prestress to the ferromagnetic composite, magnetic domains of the positive magnetostriction component switch towards the perpendicular direction, meanwhile magnetic domains of the negative magnetostriction component switch towards the parallel direction. Once a parallel magnetic field is applied, all the magnetic domains switch towards the parallel direction, for which the different domain switching pathways are linked by hollow arrows in Fig. 9. Consequently, during the whole magnetization process, the permeability keeps unchanged, as observed in Fig. 1.

In principle, this effect can be understood by considering the stress-induced magnetoelastic energy (also named as "magnetostrictive energy") for each component. The magnetoelastic energy can be expressed as

$$E_{\mathrm{me}} = 3/2\lambda_s\sigma\sin^2\theta \tag{1}$$

where $\theta$ is the angle between magnetization and stress [1,2]. Of course, this energy is in opposite sign between the two magnetostrictive phases. When a magnetic field is applied, it provides Zeeman energy

$$E_{\mathrm{H}} = -MH\cos\theta \tag{2}$$

where $\theta$ refers to the angle between external field, $H$, and magnetization, $M$. For the compressive prestress case, $E_{\mathrm{me}}$ and $E_{\mathrm{H}}$ have the same sign for the negative magnetostriction component (both the compressive stress and magnetic field switch the domains toward the parallel direction), meanwhile they have opposite signs for the positive magnetostriction component (competitive contributions on domain switching pathways between the compressive stress and the magnetic field). For the present Fe-Ga composite, the reduced permeability in the bcc-averaged sample is due to the competition between $E_{\mathrm{H}}$ and $E_{\mathrm{me}}$. The nearly unchanged permeability in the bcc + fcc Fe-Ga composite is due to the overcome of $E_{\mathrm{me}}$ of the bcc phase by $E_{\mathrm{me}}$ of the fcc phase. Of course, the case for tensile prestress is also easily understood. The permeability for the fcc phase will decrease, because the $E_{\mathrm{me}} = 3/2\lambda_s\sigma\sin^2\theta$ is against the energy $E_{\mathrm{H}} = -MH\cos\theta$. But when the bcc phase coexists, its $E_{\mathrm{me}}$ will counteract that of the fcc phase, also leading to stress-insensitive permeability during the subsequent magnetization process. In other words, the stress-induced magnetoelastic anisotropy $K_\sigma = -3/2\lambda_s\sigma$ for the negative magnetostriction component is compensated by the one for the positive magnetostriction component.

The compensation of SIAs between two components with opposite magnetostriction signs might be a recipe for design of soft magnets with stress-insensitive permeability. Unlike the usual approach through alloying nonmagnetic Si and Al or ferromagnetic Ni into Fe to obtain zero magnetostriction [12–15], we reach the same goal by *structure engineering* without changing the average composition. The magnets designed by this approach could have applications in quasistatic environments. For instance, the present Fe-Ga composite may be used as the poles of an electromagnet to conduct the magnetic field generated by the current-carrying coils. In some close-circuit magnetomechanical measurements, the poles are also used as pressure heads on the samples; they will be compressed during loading. In this case, the poles should maintain stress-insensitive magnetic permeability. More importantly, this approach may be applicable for other material systems. Since the present proof-of-principle reference Fe-Ga alloy has a higher coercivity and smaller permeability than long-established materials such as Fe-Ni alloy and Fe-Si-Al alloy, one may choose proper material systems with lower coercivity and higher permeability. In addition, $\lambda_s$ for either the bcc or fcc phase in Fe-Ga alloys is relatively large, one also may choose a composite so that the constituting components have smaller $\lambda_s$ values. Although special system selection and processing control are required to design better materials in engineering applications, the present principle may lead to ideas for designing soft magnets.

## IV. CONCLUSIONS

In summary, stress tolerant soft magnets can be developed through the compensation of stress-induced extra anisotropies between two ferromagnetic components with opposite magnetostriction signs. A Fe-Ga composite that contains a positive magnetostriction bcc phase and negative magnetostriction fcc phase can serve as a good candidate, exhibiting stable magnetic permeability and coercivity as well as high saturation magnetic induction even under 200-MPa compressive prestress. The competitive domain switching pathways under stresses and the offsetting of the stress-induced magnetoelastic energies between these two components result in these appealing stress-insensitive magnetic properties. These findings may provide a general recipe to design stress tolerant soft magnets.

## ACKNOWLEDGMENTS

This work was supported by the National Natural Science Foundation of China (Grants No. 51622104, No. 51501170, No. 51871174, No. 51831006, and No. 51431007), the Young Talent Support Plan of Xi'an Jiaotong University, and the Thousand Talents Program of Shaanxi Province. We thank

Prof. Yongmao Pei and Mr. Zengyao Lv of Peking University, and Prof. Weixing Xia of Ningbo Institute of Materials Technology and Engineering, Chinese Academy of Sciences for kind help in magnetomechanical measurements and L-TEM characterizations.

## APPENDIX: PHASE FIELD SIMULATIONS

To predict the domain switching in the present paper, a real-space phase field model for ferromagnetic materials based on the Ginzburg-Landau theory [35] is employed. The magnetization vector $M = (M_1, M_2, M_3, t)$ is chosen as the order parameter in the phase-field model. According to the fundamental thermodynamics, the domain structures are determined by the competition between different energies of the materials. The total free-energy density of the ferromagnetic material can be described by

$$E = E_{\text{anis}} + E_{\text{exch}} + E_{\text{elas}} + E_{\text{mag}} + E_{\text{cons}}, \tag{A1}$$

where $E_{\text{anis}}$, $E_{\text{exch}}$, $E_{\text{elas}}$, $E_{\text{mag}}$, and $E_{\text{cons}}$ denote the magnetocrystalline anisotropy energy density, the exchange energy density, the elastic energy density, the magnetostatic energy density, and the constraint energy density, respectively.

The magnetocrystalline anisotropy energy density for the present cubic Fe-Ga phases can be described by

$$E_{\text{anis}} = \frac{K_1}{M_s^4}\left(M_1^2M_2^2 + M_1^2M_3^2 + M_2^2M_3^2\right) + \frac{K_2}{M_s^6}\left(M_1^2M_2^2M_3^2\right), \tag{A2}$$

where $K_1$ and $K_2$ are the anisotropy constants, $M_i$ are the components of the magnetization, and $M_s$ is the magnitude of the saturation magnetization. The exchange energy density can be written as

$$E_{\text{exch}} = \frac{A}{M_s^2}\left(M_{1,1}^2 + M_{1,2}^2 + M_{1,3}^2 + M_{2,1}^2 + M_{2,2}^2 + M_{2,3}^2 + M_{3,1}^2 + M_{3,2}^2 + M_{3,3}^2\right), \tag{A3}$$

where $A$ is the exchange stiffness constant, and $M_{i,j} = \partial M_i/\partial x_j$ denotes the components of the derivative of the magnetization vector $M_i$ with respect to $x_j$. The elastic energy density contains the pure elastic energy density $E_{\text{pure}}$ and the coupling elastic energy density between magnetization and strain $E_{\text{cou}}$, which can be expressed as

$$E_{\text{elas}} = E_{\text{pure}} + E_{\text{cou}} = \frac{1}{2}c_{11}\left(\varepsilon_{11}^2 + \varepsilon_{22}^2 + \varepsilon_{33}^2\right) + c_{12}(\varepsilon_{11}\varepsilon_{22} + \varepsilon_{11}\varepsilon_{33} + \varepsilon_{22}\varepsilon_{33}) + 2c_{44}\left(\varepsilon_{12}^2 + \varepsilon_{13}^2 + \varepsilon_{23}^2\right) - \frac{3\lambda_{100}}{2M_S^2}(c_{11} - c_{12})\left(\varepsilon_{11}M_1^2 + \varepsilon_{22}M_2^2 + \varepsilon_{33}M_3^2\right) - \frac{6\lambda_{111}}{M_S^2}c_{44}(\varepsilon_{12}M_1M_2 + \varepsilon_{13}M_1M_3 + \varepsilon_{23}M_2M_3), \tag{A4}$$

where $c_{11}$, $c_{12}$, and $c_{44}$ are the elastic constants, $\varepsilon_{ij}$ is the elastic strain, and $\lambda_{100}$ and $\lambda_{111}$ are the magnetostrictive constants. The magnetostatic energy density can be expressed as

$$E_{\text{mag}} = -\frac{\mu_0}{2}\left(H_1^2 + H_2^2 + H_3^2\right) - \mu_0(H_1M_1 + H_2M_2 + H_3M_3), \tag{A5}$$

where $H_i$ is the magnetic field in materials and $\mu_0$ is the permeability of a vacuum. Equation (5) includes both the magnetostatic energy and Zeeman energy. In the simulation, the total magnetic field is obtained in the materials by solving the Maxwell equation, in which the magnetostatic field and Zeeman field are included through superposition. It is equivalent to the case when the magnetostatic field and Zeeman field are separated. In addition, to make sure the magnetization satisfies the Heisenberg-Weiss constraint, i.e., the magnitude of magnetization $\sqrt{M_1^2 + M_2^2 + M_3^2} = M_s$ is almost the same everywhere in the system, we adopt the following energy density to enforce the restriction [36]

$$E_{\text{cons}} = A_s(M - M_s)^2, \tag{A6}$$

where $M = \sqrt{M_1^2 + M_2^2 + M_3^2}$ is the magnitude of magnetization and $A_s$ is the constraint energy constant. The constraint energy is used instead of simply reducing the number of magnetic variables because it is easy to implement in the phase field model based on the finite element method.

The temporal evolution of the magnetization is described by the time-dependent Ginzburg-Landau equation

$$\frac{\partial \mathbf{M}(\boldsymbol{r}, t)}{\partial t} = -L\frac{\delta F}{\delta \mathbf{M}(\boldsymbol{r}, t)}, \tag{A7}$$

where $L$ is the kinetic coefficient, $F = \int_V E dV$ is the total free energy of the system, and $\delta F/\delta \boldsymbol{M}(\boldsymbol{r}, t)$ represents the thermodynamic driving force for the spatial and temporal evolution of the magnetization. Additionally, the mechanical equilibrium equation $\frac{\partial}{\partial x_j}(\frac{\partial E}{\partial \varepsilon_{ij}}) = 0$ and the Maxwell equation $\frac{\partial}{\partial x_i}(-\frac{\partial E}{\partial H_i}) = \frac{\partial}{\partial x_i}(B_i) = 0$ [35] are introduced to describe the evolution of elastic strain and magnetic field. In the mechanical equilibrium and Maxwell equations, the repeated indices denote the summation convention from 1 to 3.

Using the principle of virtual work, the weak form of the governing equation can be derived as

$$\int_V \left[\frac{\partial E}{\partial \varepsilon_{ij}}\delta\varepsilon_{ij} + \frac{\partial E}{\partial H_i}\delta H_i + \left(\frac{\partial M_i}{L\partial t} + \frac{\partial E}{\partial M_i}\right)\delta M_i + \frac{\partial E}{\partial M_{i,j}}\delta M_{i,j}\right]dv = \int_B \left[t_i\delta u_i - B_jn_j\delta\phi + \frac{\partial E}{\partial M_{i,j}}n_j\delta M_i\right]ds, \tag{A8}$$

in which $t_i$ is the traction on the surface, $u_i$ is the mechanical displacement, $\phi$ is the magnetic potential, $B_j$ is the normal component of the magnetic induction, and $\frac{\partial E}{\partial M_{i,j}}n_j$ is

TABLE I. The parameters used for phase field simulation [18–21,28,29,33,37].

| Phase | $K_1(\mathrm{J/m^3})$ | $\lambda_{100}$ | $M_S(\mathrm{A/m})$ | $A(\mathrm{J/m^3})$ | $A_S$ | $c_{11}(\mathrm{N/m^2})$ | $c_{12}(\mathrm{N/m^2})$ | $c_{44}(\mathrm{N/m^2})$ |
|---|---|---|---|---|---|---|---|---|
| $D0_3$ | $1.23 \times 10^4$ | $2.82 \times 10^{-4}$ | $9.91 \times 10^5$ | $6.0 \times 10^{-12}$ | 0.51 | $2.07 \times 10^{11}$ | $1.16 \times 10^{11}$ | $1.08 \times 10^{11}$ |
| $L1_2$ | $1.66 \times 10^4$ | $-2.98 \times 10^{-4}$ | $1.30 \times 10^6$ | $1.0 \times 10^{-11}$ | 0.51 | $2.05 \times 10^{11}$ | $1.68 \times 10^{11}$ | $1.32 \times 10^{11}$ |

the gradient flux of magnetization on the surface. A finite element method is employed to solve these equations. Table I summarizes the parameters of bcc and fcc Fe-Ga phases taken from Refs. [18–21,28,29,33,37].


[1] S. Chikazumi, *Physics of Ferromagnetism*, 2nd ed. (Clarendon Press, Oxford, 1997).
[2] J. M. D. Coey, *Magnetism and Magnetic Materials* (Cambridge University, Cambridge, England, 2010).
[3] D. C. Jiles, Acta Mater. **51**, 5907 (2003).
[4] G. Herzer, Scripta Metall. Mater. **33**, 1741 (1995).
[5] O. Gutfleisch, M. A. Willard, E. Brück, C. H. Chen, S. G. Sankar, and J. P. Liu, Adv. Mater. **23**, 821 (2011).
[6] M.Y. Lu, in Proceedings of the Third National Conference on High-Performance Soft Ferrites and Their Applications, 2007 (in Chinese).
[7] J. P. Joule, Philos. Mag. **30**, 76 (1847).
[8] A. E. Clark, *Ferromagnetic Materials* (North-Holland, Amsterdam, 1980).
[9] J. H. Liu, C. B. Jiang, and H. B. Xu, Sci. China, Ser. E: Technol. Sci. **55**, 1319 (2012).
[10] M. K. Devine and D. C. Jiles, J. Appl. Phys. **81**, 5603 (1997).
[11] Y. M. Pei, D. N. Fang, and X. Feng, Appl. Phys. Lett. **90**, 182505 (2007).
[12] F. Lichtenberger, Ann. Phys. (Berlin) **407**, 45 (1932).
[13] T. Miyazaki, T. Oomori, F. Sato, and S. Ishio, J. Magn. Magn. Mater. **129**, L135 (1994).
[14] M. Takahashi, H. Arai, and T. Wakiyama, IEEE Trans. Magn. **23**, 3523 (1987).
[15] T. Y. Ma, M. Yan, and W. Wang, Scripta Mater. **58**, 243 (2008).
[16] S. Guruswamy, N. Srisukhumbowornchai, A. E. Clark, J. B. Restorff, and M. Wun-Fogle, Scripta Mater. **43**, 239 (2000).
[17] O. Ikeda, R. Kainuma, I. Ohnuma, K. Fukamichi, and K. Ishida, J. Alloys Compd. **347**, 198 (2002).
[18] G. Petculescu, R. Wu, and R. McQueeney, Handb. Magn. Mater. **20**, 123 (2012).
[19] N. Kawamiya, K. Adachi, and Y. Nakamura, J. Phys. Soc. Jpn. **33**, 1318 (1972).
[20] N. Srisukhumbowornchai and S. Guruswamy, J. Appl. Phys. **92**, 5371 (2002).
[21] T. V. Jayaraman, R. P. Corson, and S. Guruswamy, J. Appl. Phys. **102**, 053905 (2007).
[22] A. G. Khachaturyan and D. Viehland, Metall. Mater. Trans. A **38**, 2308 (2007).
[23] Q. Xing, Y. Du, R. J. McQueeney, and T. A. Lograsso, Acta Mater. **56**, 4536 (2008).
[24] Y. K. He, J. M. D. Coey, R. Schaefer, and C. B. Jiang, Phys. Rev. Mater. **2**, 014412 (2018).
[25] H. D. Chopra and M. Wuttig, Nature (London) **521**, 340 (2015).
[26] Y. K. He, Y. J. Han, P. Stamenov, B. Kundys, J. M. D. Coey, C. B. Jiang and H. B. Xu, Nature (London) **556**, E5 (2018).
[27] I. S. Golovin, A. M. Balagurov, V. V. Palacheva, I. A. Bobrikov, and V. B. Zlokazov, Mater. & Design **98**, 113 (2016).
[28] J. M. Gou, X. L. Liu, K. Y. Wu, Y. Wang, S. S. Hu, H. Zhao, A. D. Xiao, T. Y. Ma, and M. Yan, Appl. Phys. Lett. **109**, 082404 (2016).
[29] T. Y. Ma, J. M. Gou, S. S. Hu, X. L. Liu, C. Wu, S. Ren, H. Zhao, A. D. Xiao, C. B. Jiang, X. B. Ren, and M. Yan, Nature Comm. **8**, 13937 (2017).
[30] V. V. Palacheva, A. Emdadi, F. Emeis, I. A. Bobrikov, A. M. Balagurov, S. V. Divinski, G. Wilde, and I. S. Golovin, Acta Mater. **130**, 229 (2017).
[31] Y. M. Pei and D. N. Fang, Rev Sci. Instr. **77**, 086101 (2006).
[32] Y. K. He, X. Q. Ke, C. B. Jiang, N. H. Miao, H. Wang, J. M. D. Coey, Y. Z. Wang, and H. B. Xu, Adv. Funct. Mater. **28**, 1800858 (2018).
[33] J. M. Gou, Master's dissertation, Zhejiang University, 2018.
[34] R. Q. Wu, J. Appl. Phys. **91**, 7358 (2002).
[35] J. Wang and J. Zhang, Int. J. Solid. & Struct. **50**, 3597 (2013).
[36] C. M. Landis, J. Mech. & Phys. Solid. **56**, 3059 (2008).
[37] L. Zheng, Ph.D thesis, Beihang University, 2008.